PHYSICAL REVIEW D **112,** 114512 (2025)

Geometric fragmentation and anomalous thermalization in cubic dimer model

Joel Steinegger,[1,*] Debasish Banerjee,[2,†] Emilie Huffman,[3,4,‡] and Lukas Rammelmüller[5]

[1]*German Aerospace Center (DLR), Institute of Frontier Materials on Earth and in Space,*
Functional, Granular, and Composite Materials, 51170 Cologne, Germany
[2]*School of Physics and Astronomy, University of Southampton,*
University Road, Southampton SO17 1BJ, United Kingdom
[3]*Department of Physics and Center for Functional Materials, Wake Forest University,*
Winston-Salem, North Carolina 27109, USA
[4]*Perimeter Institute for Theoretical Physics, Waterloo, Ontario N2L 2Y5, Canada*
[5]*TNG Technology Consulting GmbH, Munich, Germany*

(Received 15 August 2025; accepted 4 December 2025; published 24 December 2025)

While quantum statistical mechanics triumphs in explaining many equilibrium phenomena, there is an increasing focus on going beyond conventional scenarios of thermalization. Traditionally examples of nonthermalizing systems are either integrable or disordered. Recently, examples of translationally invariant physical systems have been discovered whose excited energies avoid thermalization either due to local constraints (whether exact or emergent) or due to higher-form symmetries. In this article, we extend these investigations for the case of 3D $U(1)$ quantum dimer models, which are lattice gauge theories with finite-dimensional local Hilbert spaces (also generically called quantum link models) with staggered charged static matter. Using a combination of analytical and numerical methods, we uncover a class of athermal states that arise in large winding sectors, when the system is subjected to external electric fields. The polarization of the dynamical fluxes in the direction of applied field traps excitations in 2D planes, while an interplay with the Gauss law constraint in the perpendicular direction causes exotic athermal behavior due to the emergence of new conserved quantities. This causes a geometric fragmentation of the system. We provide analytical arguments showing that the scaling of the number of fragments is exponential in the linear system size, leading to weak fragmentation. Further, we identify sectors which host fractonic excitations with severe mobility restrictions. The unitary evolution of fragments dominated by fractons is qualitatively different from the one dominated by nonfractonic excitations.

DOI: 10.1103/4kzq-t1zs

I. INTRODUCTION

Interacting quantum many-body systems are expected to thermalize under unitary time evolution when their initial states are simple Fock states. Consequently, time-evolved pure states obtained from different Fock states with the same energy density cannot be distinguished using purely local operators, even when they have different values of another local observable. To reconcile this phenomenon with the quantum mechanics of closed systems, dominated by the time-reversible Schrödinger equation, one may invoke the eigenstate thermalization hypothesis (ETH) [1–4].

The ETH may be stated in terms of the matrix elements of observables in the eigenbasis of the Hamiltonian as

$$O_{mn} = O(\bar{E})\delta_{mn} + e^{-S(E)/2} f_O(\bar{E}, \omega) R_{mn}, \qquad (1)$$

where m, n are indices for the energy spectrum E_n, $\bar{E} = (E_m + E_n)/2$, and $\omega = E_n - E_m$. Then $S(\bar{E})$ and $O(\bar{E})$ are the thermodynamic entropy and expectation value of the observable in the microcanonical ensemble at energy $\bar{E}$, respectively, f_O is a smooth function of the arguments $(\bar{E}, \omega)$, and R_{mn} are random real or complex variables with zero mean and unit variance [4]. Expectation values of local observables thus thermalize in $\mathcal{O}(1)$ time (in units of coupling) to the microcanonical ensemble due to the exponential damping offered by the entropy.

Since most systems in nature thermalize, it is interesting to understand the conditions under which systems do not.

---

[*] Contact author: joel.steinegger@dlr.de

[†] Contact author: D.Banerjee@soton.ac.uk

[‡] Contact author: ehuffman@wfu.edu

Published by the American Physical Society under the terms of the Creative Commons Attribution 4.0 International license. Further distribution of this work must maintain attribution to the author(s) and the published article's title, journal citation, and DOI. Funded by SCOAP^3.

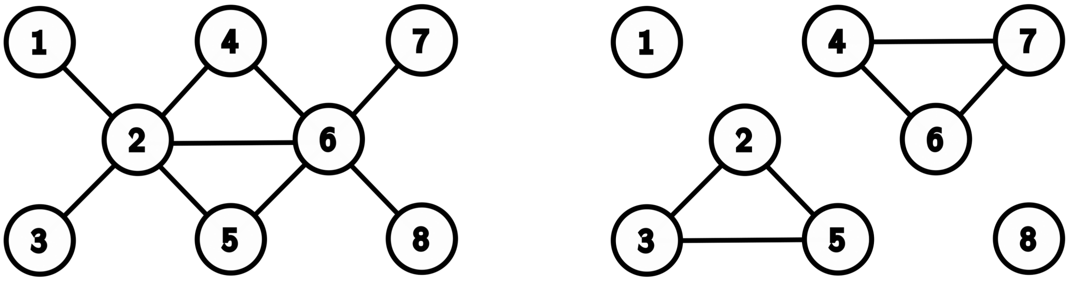

FIG. 1. Consider an example of a quantum system with eight states which cannot be further distinguished by local or global symmetries. The model is said to be "ergodic" if the Hamiltonian connects all the states (left). The same quantum system transforming under a different Hamiltonian which does not connect all the states, and the model is considered to be "fragmented" (right).

Integrable and disordered systems offer some of the well-explored routes to violate ETH [5,6]. Moreover, the initial experimental exploration of quantum dynamics on a Rydberg atom-based quantum simulator [7] led to the discovery of quantum many-body scars (QMBS) [8–10], which consist of a set of eigenstates with anomalously low entanglement entropy (and anomalous values of other observables) embedded in an otherwise ETH-satisfying spectrum. When starting from states with a high overlap with these QMBS, the unitary evolution may keep the system within the subspace of these scars, resulting in a longer thermalization time. A theoretical description of this phenomena can be obtained by modeling the system by the so-called PXP model [11], which has since been found [12] to be identical to the spin-$\frac{1}{2}$ quantum-link Schwinger model [13,14]. This has opened the door to large-scale quantum simulations of lattice gauge theories. Subsequently a plethora of nonergodic behaviors have been discovered in strongly interacting systems [15,16]. QMBS have been observed in a wide variety of physical systems from spin models [15–28] and fermionic theories [29–33], as well as in lattice gauge theories both with and without matter [34–43], and even in cases when gauge theories are disordered [44].

Another example of ETH-violating behavior arises when the Hilbert space is fragmented into sectors that cannot be distinguished by global symmetries. Certain scenarios such as disorder-free localization [45–50] sometimes can be mapped to systems with local gauge or subsystem symmetries. Therefore anomalous thermalization in such systems can be understood as an incoherent sum of different (gauge) sectors, each thermalizing at its own pace. Other scenarios such as "weak" and "strong fragmentation" are more subtle and can emerge without requiring local microscopic symmetries. To understand these scenarios, imagine that Fock states (in a suitable computational basis, or one which can be easily prepared in the laboratory) are represented as vertices of a graph, and the Hamiltonian represents the connections (bonds) of the graph. If the resulting graph is a single connected object, the system is ergodic, but if it instead is divided into disconnected sectors, the number of which grows with the system size, then the system can potentially evade thermalization as postulated by the ETH. A common terminology used in this case is to say that the system is "fragmented." The cartoon representation of Fig. 1 for a Hamiltonian connecting different states of a finite system provides an intuition regarding fragmentation.

A further distinction between fragmentation scenarios lies in whether one encounters a measure zero of ETH-violating states in the thermodynamic limit (weak fragmentation), or whether the number of fragments grows exponentially with the volume but no single fragment dominates in the thermodynamic limit (strong fragmentation) [24,51–61]. The former case is similar to QMBS leading to eventual thermalization, but the latter can display behavior distinct from QMBS scenarios, in particular the dramatically reduced mobility of excitations. A simple way to mathematically classify fragmentation is to consider the scaling of the ratio $n/\mathcal{N}$, where n is the number of states in the largest fragment (in a suitable computational basis) while $\mathcal{N}$ is the total number of states (in the same basis) in the entire Hilbert space. If this ratio approaches an $\mathcal{O}(1)$ number in the thermodynamic limit, while exhibiting anomalous behavior (e.g., QMBS states) at finite lattice sizes, the system is said to be "weakly fragmented," while if the ratio scales as e^{-aV} (where V is the volume of the system) then the system is said to be "strongly fragmented." Concretely, this can be converted to a comparison of the "entropy density," s_{frag}, of the biggest fragment with the thermodynamic entropy density, s_{tdyc}. For weak fragmentation, one has $s_{\mathrm{tdyc}} = s_{\mathrm{frag}}$ in the thermodynamic limit, while for the case of strong fragmentation, s_{tdyc} and s_{frag} differ by $a \sim \mathcal{O}(1)$.

In this article, we discuss a form of "geometric fragmentation" arising in a class of quantum many-body systems in three spatial dimensions which have local conservation laws, better known as quantum-link gauge theories. Specific examples of these models, such as quantum dimer models, have been extensively used in the quantum condensed matter community to discuss the nonmagnetic phases of electrons at low temperatures where electrons can form singlets with their nearest neighbors and are relevant as microscopic models of high-temperature superconductors [62–65]. Realized on a lattice structure consisting of corner-sharing tetrahedra (pyrochlores), such models are relevant in the physics of spin-ice compounds and spin-liquid phases in those systems [66–74]. In the context of particle physics, these quantum-link models [75–80] were proposed as generalizations of Wilson's lattice gauge theory [81,82] to develop better classical algorithms for quantum chromodynamics [83–88]. Thanks to recent experimental developments on quantum simulations and computations, these models are especially suited to be realized on near-term devices in order to study phenomena of interest in particle physics, particularly for problems which defy classical simulation techniques [13,89–94].

Most of the studies so far have concentrated on the phase diagram at zero temperature and at finite temperatures, which is natural given the available classical methods, as well as the experimentally relevant physics. However, thanks to the new tools for quantum simulation, there is an increasing interest in the conditions leading to (lack of) thermalization in these models. We show that in the presence of (large) external electric fields, magnetic excitations get trapped in two-dimensional planes hindering thermalization. We are able to use analytical techniques to characterize certain aspects of the anomalous states, while for other cases we display the athermal behavior numerically. Our starting point is the quantum dimer model on the cubic lattice. We then confine ourselves to a particular sector of the model, characterized by the largest winding number in a direction, which displays fragmentation.

The rest of the paper is organized as follows. In Sec. II, we introduce the model and discuss the constraints imposed by the three-dimensional Gauss law, as well as the global winding number symmetry that plays a crucial role in inducing geometric fragmentation. We then describe the observables used to characterize the anomalous dynamics. The concept of geometric fragmentation is introduced in Sec. III, with both its origin and nature examined in detail in Sec. III A. In Sec. III B, we explore the emergence of fractons within certain fragmented subspaces and how they give rise to athermal dynamics—both in fragments dominated by fractons and in those that are not. Finally, in Sec. III C, we present an analytical solution for the eigenstates and eigenenergies of the fractonic fragments. We conclude by summarizing our main findings and providing an outlook in Sec. IV.

II. MODEL AND OBSERVABLES

A. Doped bosonic quantum-link model

We begin by introducing the bosonic $U(1)$ Abelian quantum-link model (the fermionic version was introduced in [95]). Although we will focus on the Hilbert space structure and the real-time dynamics of the model in three dimensions, an understanding of the model in two dimensions equips the reader with the insight to appreciate the special dynamics we show later. The model is defined as follows on square and cubic lattices,

$$H = \frac{g^2}{2}\sum_{x,\hat{i}} E^2_{x,\hat{i}} - J\sum_{\square}(U_\square + U^\dagger_\square) + \lambda\sum_{\square}(U_\square + U^\dagger_\square)^2,$$

$$U_\square = U_{x,\hat{i}}U_{x+\hat{i},\hat{j}}U^\dagger_{x+\hat{j},\hat{i}}U^\dagger_{x,\hat{j}}. \tag{2}$$

The degrees of freedom of the model are defined on links joining two adjacent lattice sites and labeled with the subscript $(x,\hat{i})$, with x as a site and $\hat{i}$ as a unit vector in a spatial direction. The first term in Eq. (2) is the electric field energy (square of the electric fluxes, $E_{x,i}$), while the second term is the magnetic field energy, and the third term is the Rokhsar-Kivelson term. The latter two terms are expressed via plaquette operators, $\mathrm{U}_\square$. We will choose a computational basis which is diagonal in the electric fluxes, and thus the term linear in plaquette operators is off diagonal in this basis and will be the kinetic operator $H_{\mathrm{kin}} = \sum_\square(U_\square + U^\dagger_\square)$ while the term quadratic in the plaquette operator is diagonal in the flux basis is $H_{\mathrm{pot}} = \sum_\square(U_\square + U^\dagger_\square)^2$.

The speciality of the quantum-link formulation is that these operators can be represented by a finite-dimensional Hilbert space and are characterized by the representations of $SU(2)$ algebra. In particular, the operators satisfy the following commutation relations:

$$[E_{x,\hat{i}}, U_{y,\hat{j}}] = U_{x,\hat{i}}\delta_{x,y}\delta_{i,j}; \qquad [E_{x,\hat{i}}, U^\dagger_{y,\hat{j}}] = -U^\dagger_{x,\hat{i}}\delta_{x,y}\delta_{i,j};$$

$$[U_{x,\mu}, U^\dagger_{y,\nu}] = 2E_{x,\mu}\delta_{x,y}\delta_{i,j}. \tag{3}$$

The Hamiltonian has a local $U(1)$ symmetry generated by the local lattice Gauss law operator,

$$G_x = \sum_i (E_{x,\hat{i}} - E_{x-\hat{i},\hat{i}}); \qquad [G_x, H] = 0 \quad \text{for all } x. \tag{4}$$

This causes the many-body Hilbert space to break into exponentially many sectors, labeled by quantum numbers of the local charge, G_x. A typical choice in particle physics is to define physical states as being annihilated by the Gauss law: $G_x|\Psi\rangle = 0$, which corresponds to zero charge. In contrast, physical states of a quantum dimer model (QDM) have doped (immobile) staggered charges, mathematically represented as $G_x|\chi\rangle = Q(-1)^x|\chi\rangle$, where $(-1)^x$ is the site parity, and Q is the quanta of charge.

Any representation of the operators fulfilling Eq. (3) is allowed to define the theory. The well-known Wilson-type lattice gauge theory uses the quantum rotor as its degree of freedom, generating an infinite-dimensional representation on each of the links [82]. A finite-dimensional representation is obtained by using spin-S operators $\vec{S}_{x,\hat{i}}$ as degrees of freedom on the link, with the following identifications:

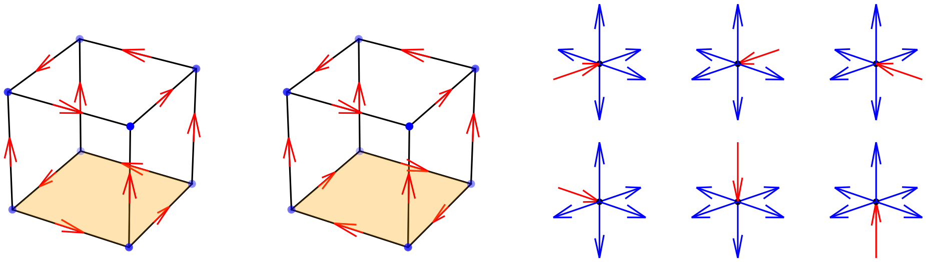

FIG. 2. An elementary cube whose top and bottom faces are flippable in the anticlockwise fashion (left). The J-term of the Hamiltonian acts on the lower (shaded) face and converts it into a clockwise flippable plaquette (middle). Hamiltonian flips preserve the local charge. (Right) States which are allowed for $Q = 2$ condition.

$$E_{x,\hat{i}} = S^3_{x,\hat{i}}; \qquad U_{x,\hat{i}} = S^+_{x,\hat{i}}; \qquad U^\dagger_{x,\hat{i}} = S^-_{x,\hat{i}}. \qquad (5)$$

In the limit of large S, the Wilson lattice gauge theory is approached [96]. In this work, we consider the other extreme limit of $S = \frac{1}{2}$ with a two-dimensional local Hilbert space and work in the electric flux basis. The electric field energy is constant in this representation and can be ignored. Working in the electric field basis, the states can be represented by flux arrows pointing outward (inward) to the site representing flux $\frac{1}{2}$ $(-\frac{1}{2})$. A pictorial representation of the action of the Hamiltonian on an individual state is given in Fig. 2. Moreover, physical states can be locally classified using the Gauss law. The number of states allowed decreases with the increase in Q: for three-dimensional cubic lattices, $Q = 0$ admits 20 states [95], $Q = 1$ allows 15 states, $Q = 2$ allows 6 states, and $Q = 3$ allows only a single state. Figure 2 shows the case of the local charge $Q = +2$. We do not draw all the states for the other Gauss law conditions, but the reader is encouraged to draw them for their understanding.

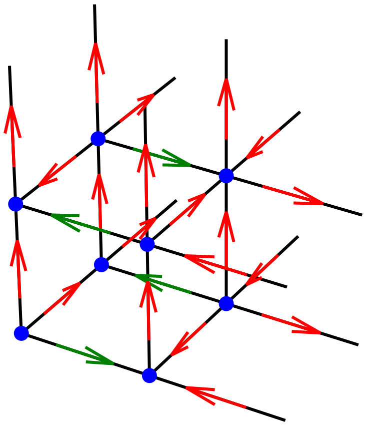

FIG. 3. An example state which maximal winding in the z-direction: $(W_x, W_y, W_z) = (0, 0, 2)$. The quantity W^{3D}_x is obtained by summing the flux contributions highlighted in green.

B. Winding number symmetry

The Hamiltonian of the system is invariant under (global) point group symmetries (rotations, reflections, and translations), as well as charge conjugation. Our work focuses on the remaining continuous global center symmetry, which gives rise to conserved flux winding number sectors. On an $L_x \times L_y \times L_z = V$ (three-dimensional) lattice with periodic boundary conditions, there are three separately conserved winding numbers $W = (W^{3D}_x, W^{3D}_y, W^{3D}_z)$,

$$W^{3D}_x = \frac{1}{L_y L_z} \sum_r E_{r,x}, \qquad W^{3D}_y = \frac{1}{L_x L_z} \sum_r E_{r,y},$$
$$W^{3D}_z = \frac{1}{L_x L_y} \sum_r E_{r,z}. \qquad (6)$$

Illustrations of the winding number calculations in 3D are shown in Fig. 3. W_i ranges in integer steps from $-L_i/2$ to $L_i/2$. Since we consider the physics for the largest winding sector in a given (z) direction, we will also need the corresponding two-dimensional winding numbers, $W = (W^{2D}_x, W^{2D}_y)$,

$$W^{2D}_x = \frac{1}{L_y} \sum_r E_{r,x}, \qquad W^{2D}_y = \frac{1}{L_x} \sum_r E_{r,y}. \qquad (7)$$

The corresponding calculation for W^{2D}_i is illustrated in Fig. 4.

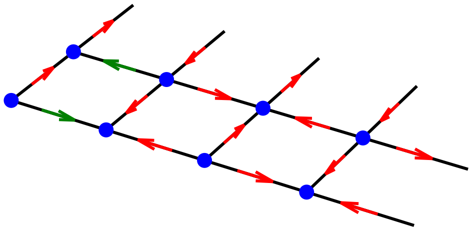

FIG. 4. Calculation of the winding number in two-dimensional planes. In this example, we have the 2×4 lattice with the winding number $(W^{2D}_x, W^{2D}_y) = (0, 0)$. The quantity W^{2D}_x is obtained by summing the flux contributions highlighted in green.

C. Time-dependent observables

Before discussing the physics of how disconnected sectors arise in these models, let us briefly mention the observables we use to track the consequences of ergodicity breaking. Since thermalization implies the loss of memory of initial conditions, a standard technique is the study of real-time dynamics of the expectation values of operators, fidelities, and measures of entanglement starting from initial states which can be *easily* prepared both theoretically and experimentally. In Sec. III B, we will examine the unitary evolution of the system, compare behaviors in different subspaces, and contrast the sectors which thermalize from those which do not. To exemplify how fragmentation leads to ETH breaking in this model and to illustrate our analytical findings about atypical dynamics of the model we numerically calculate the following time-dependent measures: the fidelity

$$F(t) = |\langle\Psi(0)|\Psi(t)\rangle|^2, \tag{8}$$

which measures the overlap with the initial state. Thermalization implies that $F(t)$ goes to zero very rapidly and typically never becomes an $\mathcal{O}(1)$ quantity. When this quantity regularly increases, some form of ergodicity breaking is suspected. The Shannon entropy, defined as

$$S(t) = -\sum_n |c_n|^2 \log_2(|c_n|^2) \quad \text{with} \quad |\Psi(t)\rangle = \sum_n c_n |n\rangle, \tag{9}$$

measures the spread of the wave function in the Fock space. Note that the numerical value is dependent on the basis chosen to label the Hilbert space (which we denote as $|n\rangle$ in a particular winding flux sector), but other (local) basis choices are still expected to show the difference between thermalizing and nonthermalizing behaviors. When started in a pure state, it is zero, but will increase to an $\sim\mathcal{O}(1)$ quantity if the wave function has support in the entire Fock space. The maximally entangled state scales as the logarithm of the total Hilbert space. Finally, we also track the evolution of kinetic and potential energy, which we label as

$$E_{\mathrm{kin}}(t) = \langle\Psi(t)|H_{\mathrm{kin}}|\Psi(t)\rangle, \qquad E_{\mathrm{pot}}(t) = \langle\Psi(t)|H_{\mathrm{pot}}|\Psi(t)\rangle. \tag{10}$$

In all our numerical examples, we start the state at $t = 0$ in one of the flux basis states of the investigated subspace: $|\Psi(0)\rangle = |n\rangle$, and use $\Delta t = 0.001$ as the time step size uniformly in all our calculations. However, since we are always using exact methods for the calculation, the value at any arbitrary time can be computed.

III. GEOMETRIC FRAGMENTATION

In the absence of any staggered static charges, i.e., in the sector characterized by $G_x = 0$, the model is expected to be ergodic for zero winding number sectors. While we are aware that this is the case in $d = 2$ [35], a similar check does not (yet) exist in $d = 3$ to the best of our knowledge. As the system is doped using staggered static charges, the allowed Gauss law realizations further constrain the set of allowed states and risk an otherwise connected Hamiltonian graph to fragment. This is even more so if the system is subjected to an external field which locks the electric fluxes in the direction of the field, but keeps those transverse to the field unaffected. In this section, we consider a particular limiting case of the quantum dimer model [i.e., where the constraint $G_x = (-1)^x$ selects the physical states and allows for 15 states locally on each site], with external electric field. This is equivalent to considering the model in the highest winding number sector in the direction of the field, for example in the sector $(0, 0, W_z^{\max})$ without any loss of generality. An example state in this sector is shown in Fig. 3. Let us now discuss how fragmentation may arise in this scenario.

A. Fragmentation in the doped quantum link model

In the maximal winding number sector of the dimer model, all the z-fluxes (in the direction of the external electric field) point in the same direction. This holds irrespective of the lattice size. In particular, this means that the spatial plaquettes in the xz-plane and the yz-plane cannot be made flippable since the z-links in each of these plaquettes always point in the same direction. Flippable plaquettes can only exist in the xy-plane. This leads to the key result that the maximal flux states can be represented as L_z stacked 2D QDMs, which stagger the charge as one moves in the z-direction at a fixed value of (x, y).

This means that we can effectively describe the basis states in the flux basis of the $(0, 0, W_z^{\max})$ sector as

$$|\Psi_{3D}\rangle = |\Psi_{2D}^1\rangle \otimes |\Psi_{2D}^2\rangle \otimes \cdots |\Psi_{2D}^{L_z}\rangle, \tag{11}$$

since the fluxes in the z-direction are fixed. The effective Hamiltonian reduces to a sum of operators only acting on the xy planes,

$$H = H_1^{2D} \otimes \mathbb{1}^{\otimes(L_z-1)} + \mathbb{1} \otimes H_2^{2D} \otimes \mathbb{1}^{\otimes(L_z-2)} + \cdots + \mathbb{1}^{\otimes(L_z-1)} \otimes H_{L_z}^{2D}. \tag{12}$$

The Hamiltonian can be taken to be 1 for the terms in the xz- and yz-planes since their plaquettes are not flippable by construction. Furthermore, the effective 2D QDMs must be stacked in a pattern such that the correct winding sectors W_x^{3D} and W_y^{3D} are reproduced. This is responsible for creating a further constraint in the perpendicular directions even though the external field does not directly affect E_x and E_y links. The winding number for a direction i, W_i^{3D}, is obtained by adding the ith flux through a plane perpendicular to i. On the other hand, W_i^{2D} is obtained

TABLE I. Winding subspaces of a 2 × 4 QDM. Fractons are plaquette excitations which have reduced mobility along subdimensional manifold than the one in which the Hamiltonian is defined.

W_x	W_y	No. states	Fractons
2	0	1	✗
−1	0	8	✓
0	−1	1	✗
0	0	16	✗
0	1	1	✗
1	0	8	✓
2	0	1	✗

by summing the E_i along a line perpendicular to the links. Therefore, we can calculate the winding number of $|\Psi_{3D}\rangle$ by summing the winding numbers of L_z stacked 2D QDMs,

$$W_x^{3D} = \sum_{i=1}^{L_z} W_{x,i}^{2D}, \qquad W_y^{3D} = \sum_{i=1}^{L_z} W_{y,i}^{2D}. \tag{13}$$

In the maximal winding sector $(W_x, W_y, W_z^{\max})$, this provides a way to identify the new conserved quantity, W_i^{2D}, since W_i^{2D} of the 2D planes cannot change by applying the Hamiltonian. The only flippable plaquettes are in the xy-planes which cannot communicate via frozen E_z fluxes on the xz- and the yz-planes. It is important to realize this is not the case for states in arbitrary winding number states in 3D and is not due to a global symmetry of the Hamiltonian. Particularly, if we can fulfill Eq. (13) with different combinations of 2D QDM planes, they would not be connected by the Hamiltonian. This results in geometric fragmentation of the Hilbert space. Naively, one may think that this always implies fragmentation for maximal flux in one direction, but there is no guarantee that there exist at least two ways to fulfill Eq. (13). To predict fragmentation definitively, we must also obtain winding subspaces of an arbitrary lattice of size $L_x \times L_y \times L_z$ consisting of states that fulfill Eq. (13) in at least two different ways. In Supplemental Material [97], we analytically prove this to be the case for a large class of examples.

In the main text, let us instead show how this arises by simple examples. Consider the 4 × 2 × 2 lattice in the winding sector $W^{3D} = (1, 1, 4)$: this is fragmented into two subspaces, each consisting of eight states. Table 1 shows the subspaces of the QDM alongwith the number of states in each. The geometry makes the system be treated as two parallel alternating dimer planes of size 2 × 4, which have to fulfill Eq. (13). An example of this effective representation for the 2 × 2 × 2 lattice is shown in Fig. 5. To fulfill these equations with states depicted in Table 1, there are only two ways:

(1) $W_x^{2D} = 1$ and $W_y^{2D} = 0$ for the first plane, and $W_x^{2D} = 0$ $W_y^{2D} = 1$ for the second plane

(2) $W_x^{2D} = 0$ and $W_y^{2D} = 1$ for the first plane, and $W_x^{2D} = 1$ $W_y^{2D} = 0$ for the second plane.

From here we see that the sector is fragmented into two subspaces. In both solutions, one plane contains eight possible states, and the other plane contains one possible state, resulting in the fact that both subspaces have eight states as predicted by a brute-force numerical calculation, where we construct the Hamiltonian graph for the Fock space and check the number of connected components. Therefore, the numerical example matches our maximal-flux description of how fragmentation occurs. Similarly, in the sector (1,4,1), one finds a similar fragmentation, as is of course predicted by symmetry. It is instructive to consider the winding sector $W^{3D} = (3, 0, 2)$ of the 2 × 2 × 4 lattice as a second example. This winding subspace is fragmented

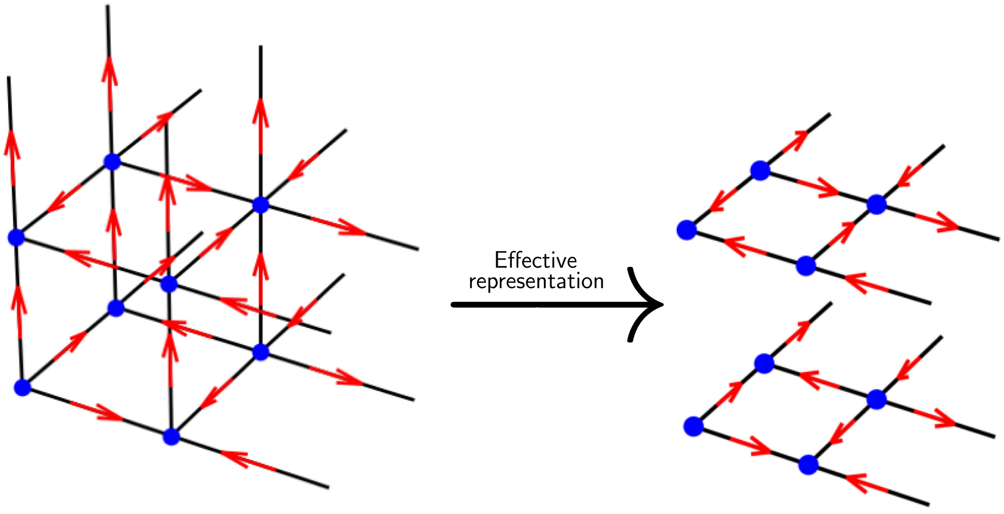

FIG. 5. When the winding numbers are maximal in a given direction, it is possible to represent the states as 2D planes since the dynamics is frozen in the perpendicular direction of the plane.

TABLE II. Winding subspaces of a 2×2 QDM. Fractons are plaquette excitations which have reduced mobility along subdimensional manifold than the one in which the Hamiltonian is defined.

W_x	W_y	No. states	Fractons
−1	0	1	✗
0	−1	1	✗
0	0	4	✓
0	1	1	✗
1	0	1	✗

into four distinct sectors, each containing four 3D quantum dimer model (QDM) states. Due to the geometry of the system, each state can be interpreted as comprised of four parallel, alternating dimer planes of size 2×2, each subject to the constraints imposed by Eq. (13). There exist four distinct ways to satisfy these constraints using distinct 2×2 subspaces of the 2D QDM. The possible subspaces of the 2×2 QDM are shown in Table II. The construction begins by selecting one of the four planes to host a configuration with winding numbers $W_x^{2D} = 0$ and $W_y^{2D} = 0$, while assigning $W_x^{2D} = 1$ and $W_y^{2D} = 0$ to the remaining planes. Since there are four possible choices for the plane in the $W_x^{2D} = 0$, $W_y^{2D} = 0$ configuration, this results in four distinct fragments, each containing four states, within the subspace.

Next we analyze the type of fragmentation—strong or weak—that emerges due to geometric constraints induced by maximal flux along a single direction in a 3D QDM. To quantify the nature of this fragmentation, we consider the following ratio in the thermodynamic limit ($L \to \infty$) of the cubic lattice $L \times L \times L$:

$$\mathcal{F} = \lim_{L\to\infty} \frac{N_{\text{largest}}}{N_{\text{total}}} \tag{14}$$

where N_{largest} denotes the number of states in the largest fragment within a given fragmented winding sector, and N_{total} is the total number of states in that winding sector. If this quantity scales as $\exp(-V)$, the system exhibits strong fragmentation, otherwise we will claim weak fragmentation.

In the main text of this work, we concentrate on the winding sector $(0, 0, W_z^{\max})$ specifically to characterize the nature of its fragmentation. Based on the construction of stacking L_z 2D lattice planes along the z-direction, it follows directly that the largest fragment within this winding sector corresponds to stacking L_z copies of the $(W_x^{2D}, W_y^{2D}) = (0, 0)$ sector on top of one another in a lattice of size $L_x \times L_y \times L_z$. Let us say the number of states in the 2D $(W_x^{2D}, W_y^{2D}) = (0, 0)$ sector is n_0. It follows that $N_{\text{largest}} = n_0^{L_z}$. Our approach involves establishing upper and lower bounds on $\mathcal{F}$ [Eq. (14)]. The key problem with evaluating the scaling of $\mathcal{F}$ is that N_{total} (total number of states across all fragments) is not easily computable since we are dealing with a constrained model in the thermodynamic limit. Thus we will instead find the scalings of two numbers: $N_{\min}$ which is a known subset of the total number of states and thus always smaller than N_{total}, and $N_{\max}$, which is by construction larger than N_{total} for all L. We thus will have $N_{\min} < N_{\text{total}} < N_{\max}$ for all L.

For $N_{\min}$, we note that, in the thermodynamic limit, 2D lattice planes in the following five winding number sectors (0,0), $(0, \pm 1)$ and $(\pm 1, 0)$ have the same number of Fock states. To satisfy $W_x^{3D} = 0$, we can combine $L_z/2$ pairs of 2D planes, such that *both* elements of a single pair have (0,0) windings or one plane has (1,0) and the other $(-1, 0)$ winding (similarly for y-windings). Further, $n_1 \approx n_0$, where n_1 is the number of states in the (1,0) winding sector (similarly for the y-winding). Thus, $N_{\min} \approx n_0^{L_z} 5^{\frac{L_z}{2}}$ (the solutions along the x- and y-directions are independent) and we can form an *upper* bound by only considering these subsets of allowed solutions to the winding constraints,

$$\lim_{L\to\infty} \frac{N_{\text{largest}}}{N_{\text{total}}} < \mathcal{G}_{\text{upper}} = \lim_{L\to\infty} \frac{N_{\text{largest}}}{N_{\min}} = \lim_{L\to\infty} e^{-L\frac{\ln(5)}{2}}. \tag{15}$$

On the other hand, we can obtain an $N_{\max}$ by overcounting the number of allowed solutions, by including all the winding sectors (there are $L + 1$ of them in each direction) and assuming that each 2D winding sector has the same number of states $\approx n_0$, when in reality the number of states in the sector decrease with the winding of the sector. Thus, $N_{\max} \approx n_0^{L_z} (L + 1)^{2\frac{L_z}{2}}$, where $L = L_z$ and L_z has been written out to show the pairing. This yields a lower bound $\mathcal{G}_{\text{lower}}$,

$$\lim_{L\to\infty} \frac{N_{\text{largest}}}{N_{\text{total}}} > \mathcal{G}_{\text{lower}} = \lim_{L\to\infty} \frac{N_{\text{largest}}}{N_{\max}} = \lim_{L\to\infty} e^{-L\ln(L+1)}. \tag{16}$$

Evaluating the entropy density (where the total entropy is logarithm of the number of states), we find that the leading correction to the value in the thermodynamic limit is $\mathcal{O}(1/L^2)$ in the former case and $\mathcal{O}(\ln(L)/L^2)$ in the latter case. Since the leading correction vanishes as $L \to \infty$, the entropy density of the biggest fragment is the same as that of the full theory, and thus we classify this scenario as weak fragmentation. The actual behavior of the leading correction in our model is in between these limits, but will also go as $\mathcal{O}(\alpha/L^2)$, where α has a weaker dependence on L than a logarithm.

We emphasize that this leading behavior is different from that of models which are expected to thermalize according to the ETH. For example, the spin-$1/2$ antiferromagnetic Heisenberg model on the cubic lattice only has the total magnetization as the global conserved quantity. If one considers the ratio of the entropy density in the largest magnetization sector (which has $L^3/2$ spins with $S_z = 1/2$

and the other $L^3/2$ spins with $S_z = -1/2$), the leading correction decays as $\mathcal{O}(1/L^3)$, *faster* than the case of the 3D quantum dimer model we have presented. Intuitively, the weak fragmentation in our case is a consequence of a genuine 3D system fragmenting into individual 2D planes, with the excitations only confined within the 2D planes.

It can be shown that this plane pairing argument is enough to predict the exact leading correction to the thermodynamic limit. More precise upper and lower bonds could be made by establishing a scaling behavior of $\frac{n_f(W)}{n_0}$ where n_f is the number of states in an arbitrary winding W sector of 2D $L \times L$ lattice, but we consider this unnecessary for our present purpose. Furthermore, similar arguments can be made for other winding sectors of this model if the amount of flux in one direction is maximal ($|W_i^{3D}| = L_j \cdot L_k/2$). We find that these sectors are also weakly fragmented. The proof of the weak fragmentation is provided in Supplemental Material [97].

B. Real-time dynamics and thermalization

In Sec. I, we pointed out that unitary dynamics provides another way to diagnose the presence of ETH-violating behavior—geometric fragmentation in our case. The system initialized in one of the fragmented subspaces would thermalize slowly (or not at all in certain cases), requiring times much greater than $\mathcal{O}(1)$ time than expected if fragmentation were absent. In some cases, this ETH-violating behavior can be related to the existance of quasiparticles, called fractons, with restricted mobility. We start this subsection by developing an analytical understanding of fractons in certain fragmented spaces. Using the (non)existance of fractons, we can characterize the real-time dynamics for the 3D QDM with maximal flux in a given direction into two different categories. We contrast the dynamics for a fragmented sector of the model to another sector which thermalizes according to the prediction of ETH.

1. Fragmented subspaces

In Sec. III A, we established fragmentation in the maximal winding sector (in a particular direction). Geometric fragmentation arose in this model due to the stacking of 2D lattices containing "confining magnetic excitations," while the interlayer fluxes are frozen. The mobility of the magnetic excitations are highly restricted, as we show below, and these are the fractons of this model. We begin by identifying the winding sectors in 2D lattices containing fractons and study how their presence influences the dynamics of the stacked lattices.

For the 2D QDM with periodic boundaries and of size $L \times (nL + 2)$, where $n \in \mathbb{N}_0$, we find that the winding sector characterized by $|W_y^{2D}| = L - 1$ and $|W_x^{2D}| = n$ exhibits a highly nontrivial structure and supports only severely constrained dynamics. By symmetry, an analogous result holds for the sector with exchanged indices. The topology of the electric fluxes is such that configuration in this sector contains exactly two flippable plaquettes sharing a common link [see for example Fig. 4 (left)]. Starting from either of the two flippable plaquettes, which are the two fractons in this case, the kinetic term of the Hamiltonian acting on any initial state leads to a sequence of states where one of the flippable plaquettes in the pair move diagonally. Due to periodicity, this fracton pair cycles through the entire lattice and returns to the initial state after exactly $L \times (nL + 2)$ flips. As a result, this 2D winding space class is especially interesting due to its atypical structure and the emergence of strongly frustrated dynamics. This structure naturally influences the dynamics of the 3D model.

The construction of the states in the aforementioned winding spaces follows the specific structure described next and gives rise to frustrated dynamics. Understanding the construction helps to quantify the allowed dynamics analytically. Consider the specific example of $n = 0$ and $L = 4$, which is the 4×2 lattice, shown in the left panel of Fig. 6. We begin with a configuration in which an S-shaped flux loop (in thick orange) is drawn at the lower left edge which connects through periodic space by traversing the lattice in both the x- and y-directions. Two successive plaquette flips on plaquettes marked by a cross in the left and middle of Fig. 6 return the system to the original configuration, translated spatially in x and y direction each by a single lattice spacing. As a result, the entire subspace is spanned by only two distinct states, up to a spatial translation of fluxes consistent with the background charge distribution.

It is instructive to examine now the case $L = 4$ and $n = 1$ in more detail. This choice corresponds to a 4×6 lattice. As a representative case (among four symmetry-related winding spaces), we focus on the winding sector $W_y^{2D} = 1$, $W_x^{2D} = -1$. The leftmost panel in Fig. 7 is the

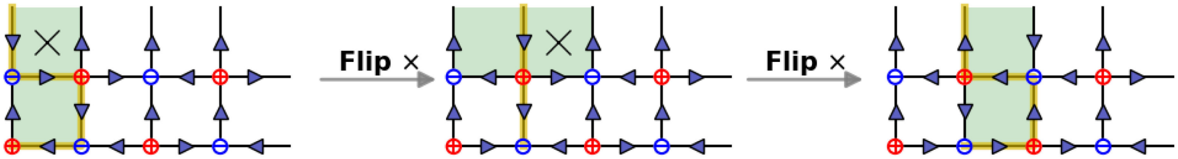

FIG. 6. Inchworm motion of the flippable plaquettes across the entire 2D plane, the two flippable plaquettes are fractions with limited mobility.

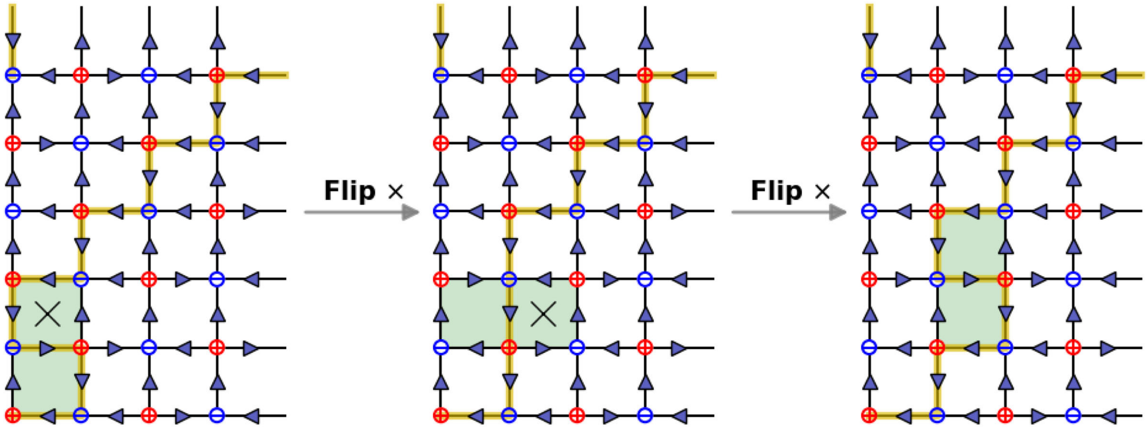

FIG. 7. The inchworm motion of fractons on the 4×6 lattice.

starting state of our construction of this winding space. In orange, one can see a flux loop connected through periodic two-dimensional space that, except for an S-shape in the lower left corner, has a "staircase" structure through the lattice. The fluxes forming the flux loop fully constrain the rest of the configuration. Given the periodic boundary conditions, the winding numbers, and the staggered charges, this is the only compatible flux pattern on the remaining links. Flipping the plaquette marked with a black cross results in the state in the middle panel of Fig. 7. One can see that there remain two flippable plaquettes sharing a link, but now they are horizontal neighbors. Flipping the plaquette marked with a black cross results in the state shown on the rightmost panel Fig. 7 where flippable plaquettes are again vertical neighbors and simply related to the state in the leftmost panel via a lattice translation in the x- and y-direction each. Subsequent flips lead to a staircaselike movement of the fracton (the flippable plaquette pair) through the 2D plane, which resembles a worm crawling along a line, and hence we dub it as the "inchworm" motion. The whole winding subspace can thus be described by two states up to a translation. Constructing the states for $n > 1$ involves addition of a staircase of directed flux to be able to close the flux loop. For $L = 4$ and $n = 2$, this is illustrated in Supplemental Material [97].

It is now clear how for arbitrary L and n this construction can be extended: we start with the S-shape flux line in the lower left corner and close the flux-loop by drawing n staircaselike flux lines through the lattice. The remaining fluxes are fixed by this construction due to the Gauss law and the 2D winding numbers (example for $n = 2$ and $L = 4$ in Supplemental Material [97]). The three additional winding sectors, related by symmetry, can be easily constructed. These sectors are obtained by either starting with an inverted S-shape flux line at the lower left corner (corresponding to a start of the flux line at a positive charge), by initiating the S-shape one site shifted in the x-direction (start from the negative charge), or by combining both modifications (i.e., a shift and an inverted S-shape). The inverted configuration results in a staircase-like motion that is also inverted (mirrored) about the y-axis, while initiating the construction from the negative charge leads to a reversal in the direction of the flux line. Illustrative examples of these constructions for the case $L = 4$, $n = 1$ are provided in Supplemental Material [97]. We emphasize the severely restricted mobility of these excitations: even though the parent system has a three-dimensional extent, these excitations can only propagate along a single line cutting across the diagonal.

The winding sectors discussed above exhibit highly unconventional dynamics, characterized by the emergence of fractons. While the behavior of these excitations is already of considerable interest in the purely two-dimensional setting, we do not pursue a detailed analysis in this work. Instead, we take a step further by connecting these findings to our results on fragmentation in the three-dimensional case and the associated conservation of winding numbers. In the fragmented regime, the 3D lattice effectively consists of decoupled stacks of 2D layers, within which the 2D winding numbers remain conserved. Consequently, the system's evolution is confined within these 2D winding sectors. We identify two distinct classes of fragmented subspaces, each exhibiting a characteristic dynamics as the system is evolved in real time:

(i) The "fractonic" fragmentation class is one where at least one fragment of the winding subspace can be understood in terms of the motion of planar fractons. Certain fragments in this category can be constructed by stacking 2D lattices whose basis states are related by the constrained motion of planar fractons, while there might exist other fragments which contain at least one 2D layer where the dynamics are not governed by planar fractons. The fragments that can be described by layers of moving fractons have $E_{\mathrm{pot}}(t) = \mathrm{const}$ and $E_{\mathrm{kin}}(t) = 0$ for all starting states, because the total number of flippable plaquettes cannot change. Due to the constrained motion, we observe even stronger resistance to thermalization and large oscillations in entropy and fidelity in time. We consider cases where some 2D layers are frozen in a fragment and all the others are constructed by 2D planes hosting fractons. Since the frozen layers do not add any dynamics, the entire dynamics are from the layers with fractions.

(ii) The "nonfractonic" fragmentation class is defined by the absence of fragments with *only* fracton-dominated 2D layers. The dynamics in each fragment is constructed by 2D layers, such that at least one layer does not allow fractons. Thus, all ways to stack the 2D subspaces have at least one subspace without a constant number of flippable plaquettes. We want to highlight that this class can, but not necessarily has, to support fractons. Here, the $E_{\mathrm{pot}}(t)$ and the $E_{\mathrm{kin}}(t)$ are not constant in time for any of the starting states. This class also shows resistance to thermalization.

We now illustrate the behavior of each of the fragmentation classes concretely through examples. In each example, we show how the 3D winding numbers can be satisfied by stacking 2D lattices and then show results of real-time dynamics initialized from a product state in the respective fragmented sector. Our numerical examples focus on lattices that extend over two sites in two directions and four sites in the remaining direction. For these system sizes, full exact diagonalization is feasible. In such lattices, the maximal winding number magnitude depends on the lattice extent: if a direction spans two sites, the maximal flux is $\max(|W_i^{3D}|) = 4$, whereas if it spans four sites, the maximum is $\max(|W_i^{3D}|) = 2$. We construct states according to the conventions described in Sec. III A, and we choose the maximal flux to be along the z-direction. Depending on whether the maximal extent of the lattice is along z, the construction involves stacking either four 2×2 lattices (corresponding to $|W_z^{3D}| = 2$) or two 4×2 lattices (corresponding to $|W_x^{3D}| = 4$). The available winding sectors for each lattice geometry are summarized in Tables I and II, where we also indicate whether the corresponding 2D winding sector contains fractons.

Let us start with a very special example of a fractonic fragmentation class, the $(W_x, W_y, W_z) = (0,0,2)$ sector of the $2\times 2\times 4$ lattice. There are 36 states that have no flippable plaquettes (each a frozen subspace), one big fragmented subspace that consists of 256 states, and 24 small fragmented subspaces each consisting of 16 states. This sector is constructed by stacking four 2×2 lattices in the z-direction such that

$$W_x^{3D} = \sum_{i=1}^{4} W_{x,i}^{2D} = 0 \quad \text{and} \quad W_y^{3D} = \sum_{i=1}^{4} W_{y,i}^{2D} = 0. \tag{17}$$

There are multiple ways to do this:

1. Four $(W_x^{2D}, W_y^{2D}) = (0,0)$ 2D winding sector lattices stacked above each other. This corresponds to the big fragment with 256 states.
2. Two $(W_x^{2D}, W_y^{2D}) = (0,0)$ winding sector lattices stacked with one $(W_x^{2D}, W_y^{2D}) = (0,1)$ winding sector lattice and one $(W_x^{2D}, W_y^{2D}) = (0,-1)$ winding sector lattice. There are 12 ways to stack these four planes above each other. Each sector has 16 states coming from the ones in the 2D planes with zero winding.
3. Two $(W_x^{2D}, W_y^{2D}) = (0,0)$ winding sector lattices and one $(W_x^{2D}, W_y^{2D}) = (1,0)$ winding sector lattice and one $(W_x^{2D}, W_y^{2D}) = (-1,0)$ winding sector lattice. There are 12 ways to stack these four planes above each other, each with 16 states.
4. Finally, there are 36 different ways to stack $(W_x^{2D}, W_y^{2D}) = (1,0)$ and $(W_x^{2D}, W_y^{2D}) = (-1,0)$, $(W_x^{2D}, W_y^{2D}) = (0,-1)$ and $(W_x^{2D}, W_y^{2D}) = (0,1)$ 2D planes above each other and fulfill Eq. (17). These are not interesting because in these are only 2D lattices without flippable plaquettes stacked above each other.

From the above classification, it follows that taking an initial state in any of these sectors and then doing an unitary time evolution maintains a constant potential energy. Because the total energy must also be constant in time, their kinetic energies are constant in time as well. All nonfrozen fragments are completely described by the dynamics of fractons.

Figure 8 summarizes the dynamics for our four measures of interest. As expected, the states without flippable plaquettes corresponding to construction 4 (blue line) do not change in time, their fidelity is always equal to 1, and their entropy, kinetic energy, and potential energy are always equal to 0. The behavior in time for all four measures of the states within the winding sector fragments is identical regardless of the starting state. The small subspaces (solid purple line) and the big subspace (solid orange line) show oscillations in the fidelity and the entropy each with a constant amplitude and period, so thermalization is evaded. All fragments are described by the dynamics of planar fractons and the fragments only differ in the amount of frozen 2D subsystems.

Another example of the fractonic fragmentation class is the $(W_x, W_y, W_z) = (1,0,4)$ sector of the $2\times 4\times 2$ lattice. In this winding sector, there are two large fragmented spaces with 128 states each, and two small ones of 8 states each. The sector is constructed by stacking two 2×4 lattices in the z-direction such that

$$W_x^{3D} = \sum_{i=1}^{2} W_{x,i}^{2D} = 1 \quad \text{and} \quad W_y^{3D} = \sum_{i=1}^{2} W_{y,i}^{2D} = 0. \tag{18}$$

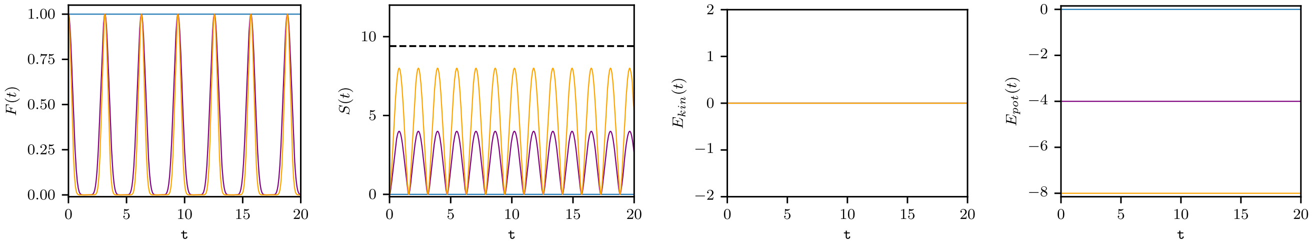

FIG. 8. Real-time dynamics of the "fractonic fragmentation class," for the case of the (0, 0, 2) sector of the $2 \times 2 \times 4$ lattice. The figures plot fidelity, Shannon entropy, the kinetic and the potential energy, from left to right.

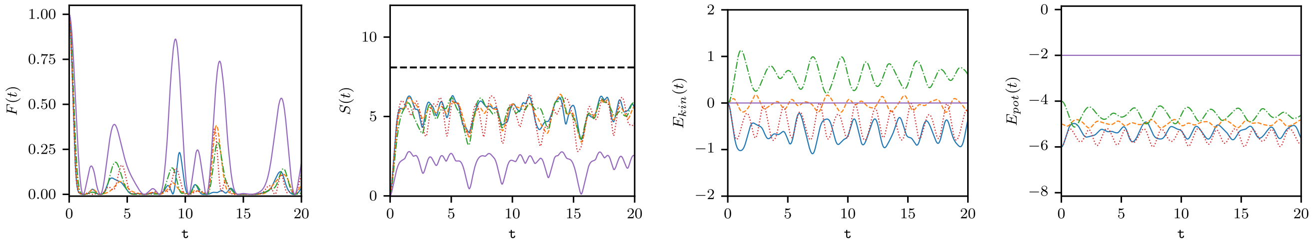

FIG. 9. Real-time dynamics of the fractonic fragmentation class (example 2). Once again, from left to right, the behavior of the fidelity, the Shannon entropy, kinetic and potential energies are shown. The athermal nature of the evolution is evident in the persistent oscillations that do not decay with time.

The fragmented subspaces are formed specifically by stacking:

(1) One $(W_x^{2D}, W_y^{2D}) = (1,0)$ plane and one $(W_x^{2D}, W_y^{2D}) = (0,0)$ plane. There are two ways to do this stacking.

(2) One $(W_x^{2D}, W_y^{2D}) = (2,0)$ and plane and one $(W_x^{2D}, W_y^{2D}) = (-1,0)$ plane, and again there are two ways to do the stacking.

The results are shown in Fig. 9. We observe four distinct types of behaviors in the large subspaces, whereas in the small subspaces (purple line), the behavior is independent of the starting state. In all subspaces we observe oscillations in the entropy and the fidelity: the entropy does not approach a steady state and the overlap with the initial wave function does not settle at zero. These oscillations are larger in the two small fragmented spaces. None of them thermalize according to ETH—note that for all of them the fidelity is significant even for very late times, and the Shannon entropy is far from the one a maximally entangled state would possess. In the large subspaces, the expectation values of the kinetic and potential energy fluctuate in time, whereas in the small subspaces the expectation value of the kinetic energy is zero and the potential energy is constant in time. These are the fragments where all 2D subsystems are described by planar fractons and their dynamics.

An example winding space that is part of the nonfractonic fragmentation class is given by the $(W_x, W_y, W_z) = (0,1,4)$ sector. We want to highlight again that this is still a fragmented sector, but it does not have fragments completely dominated by fractons. This sector consists of two different fragmented subspaces each consisting of 16 states. This sector is constructed by stacking two 2×4 lattices in the z-direction such that

$$W_x^{3D} = \sum_{i=1}^{2} W_{x,i}^{2D} = 0 \quad \text{and} \quad W_y^{3D} = \sum_{i=1}^{2} W_{y,i}^{2D} = 1. \tag{19}$$

The only way to obtain these winding numbers is by stacking one plane with $(W_y^{2D}, W_z^{2D}) = (0,0)$ and one lattice plane with $(W_y^{2D}, W_z^{2D}) = (0,1)$. There are obviously two different possibilities to do this construction. We then observe four different evolution behaviors in each of the fragments depending on the starting state. Because the 2D subspaces that are stacked above each other do not have a constant number of flippable plaquettes, the potential energy is not constant in time, and thus the kinetic energy will change in time as well. No fragment is described by planar moving fractons stacked above each other. The four measures we computed are shown in Fig. 10. All time-evolved states show fluctuations in the fidelity and the entropy. The entropy does not approach a steady value and the fidelity does not continuously go to zero. In this winding space, the expectation values of the kinetic and the potential energy are not constant, but fluctuate in time. The behavior is not independent of the starting state. Still we do not observe full thermalization and see continued fluctuations in the entropy and fidelity in time, unlike what is predicted by ETH.

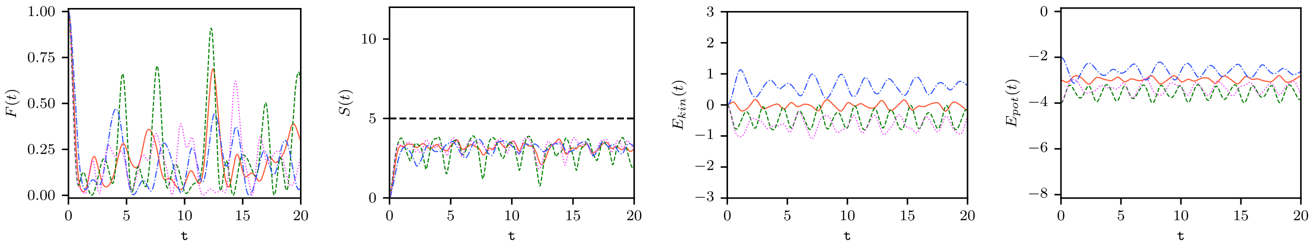

FIG. 10. Real-time dynamics for the nonfractonic fragmentation class. From left to right, the behavior of the fidelity, the Shannon entropy, kinetic and potential energies are shown. Even though fractons do not dominate this class of fragments, the persistent oscillations do not decay with time indicating athermal behavior.

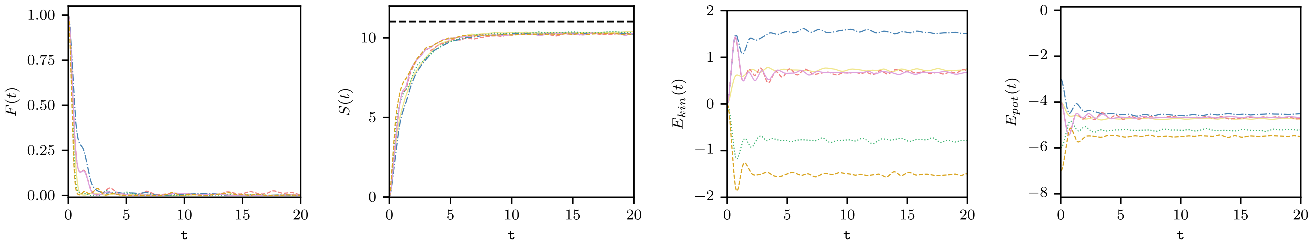

FIG. 11. Real-time dynamics of nonfragmented subspaces: clear indications of saturation observed in overlap fidelity, Shannon entropy, kinetic and potential energies (from left to right) as the system evolves unitarily in time.

2. Nonfragmented subspaces

We expect the nonfragmented subspaces to thermalize. As an example of a nonfragmented subspace of the $2 \times 2 \times 4$ lattice, we choose the $(W_x, W_y, W_z) = (2, 2, 1)$ subspace. This subspace does not have maximum flux in any direction and consists of 2084 states that are connected to each other by the Hamiltonian. We show the defined measures for nine random states of this subspace in Fig. 11. The fidelity goes to nearly zero very fast and does not increase, and the entropy rises until it saturates near the maximal entropy value (indicated as dotted black line), which indeed indicates that the system thermalizes.

C. Analytical solutions in the fractonic fragments

Here we give analytical solutions of the eigenstates and the eigenvectors for fragments that are completely dominated by planar fractons. We begin by investigating the 2D subspaces, because then Eqs. (11) and (12) will make it trivial to construct the 3D eigenstates and eigenvalues from those in 2D. Consider a lattice $L_x \times L_y = L \times (nL + 2)$, with $n \in \mathbb{N}_0$, in a winding sector defined by $|W_y^{2D}| = L - 1$ and $|W_x^{2D}| = n$. The subspace has $N = L_x \cdot L_y$ flux states, and each flux state has two flippable plaquettes with average potential energy $\alpha = -2\frac{\lambda}{J}$. Each flux state is connected by the Hamiltonian to exactly two other flux states. By choosing the right order of the flux states, this results in the following matrix representation of the Hamiltonian:

$$H^{2D}_{\text{fracton}} = \alpha \mathbb{I}_{N\times N} + C_N, \tag{20}$$

where $\mathbb{I}_{N\times N}$ is the identity matrix and C_N the adjacency matrix of the undirected cycle graph of N nodes

$$C_N = \begin{bmatrix} 0 & 1 & 0 & 0 & \cdots & 0 & 1 \\ 1 & 0 & 1 & 0 & \cdots & 0 & 0 \\ 0 & 1 & 0 & 1 & \cdots & 0 & 0 \\ 0 & 0 & 1 & 0 & \cdots & 0 & 0 \\ \vdots & \vdots & \vdots & \vdots & \ddots & \vdots & \vdots \\ 0 & 0 & 0 & 0 & \cdots & 0 & 1 \\ 1 & 0 & 0 & 0 & \cdots & 1 & 0 \end{bmatrix}. \tag{21}$$

Because the identity matrix commutes with every matrix (and hence also with C_N), it is sufficient to diagonalize C_N to calculate the eigenenergies and eigenstates. The identity matrix introduces an absolute shift by α in the eigenenergies. It is a well-known fact (e.g., [98]) that the adjacency matrix of the cycle graph is circulant with eigenvectors given by the discrete Fourier basis

$$|\lambda_j\rangle = \frac{1}{\sqrt{N}}(1, \omega^j, \ldots, \omega^{(N-1)j})^T \tag{22}$$

with $\omega = e^{2\pi i/N}$, $j = 0, \ldots, N-1$ and the eigenvalues are

$$\lambda_j = 2\cos(2\pi j/N). \tag{23}$$

Therefore, the eigenenergies are $e_j = \alpha + \lambda_j$.

It is now trivial to construct the eigenspectrum and eigenvectors of the fracton-dominated fragments. Given L_z number of stacked $L_x \times L_y$ 2D planes dominated by fractons, the eigenvectors of the effective Hamiltonian (12) are all possible combinations of the eigenstates of the 2D subsystems,

$$|E_{\{j\}}\rangle = \bigotimes_{l=1}^{L_z} |\lambda_{j_l}\rangle \tag{24}$$

and the eigenenergies are the sum of the eigenenergies of the chosen eigenstate for each combination,

$$E_{\{j\}} = \sum_{l=1}^{L_z} e_{j_l}. \tag{25}$$

The actual eigenvalues clearly depend on N. For stacking 2×2 planes, $N = 4$, which gives rise to the beating motion in Fig. 8. Other examples such as Fig. 9 have larger values of N (e.g., $N = 8$ for the purple line in the figure) and give rise to more frequencies. The crucial point is that no matter how large the lattices are, such frequencies are always present leading to athermal behavior.

IV. CONCLUSION AND OUTLOOK

While paradigms behind static properties of strongly correlated matter have acquired a maturity both in condensed matter and high-energy physics (even though novel phenomena are frequently reported), the analogous state of the field of nonequilibrium physics is still in its infancy. Understanding fragmentation, its causes, and its consequences, is indeed among the most challenging questions in the field.

Gauge theories possess constrained Hilbert spaces due to local symmetries, which are not enough to render the models integrable. Exotic behavior is obtained when matter and gauge fields strongly interact and cannot be treated nonperturbatively, and very few analytical results can be obtained. In this article, we are able to construct a limiting case of a global symmetry in the cubic dimer model where many more emergent subsystem symmetries are generated. These cause a geometric fragmentation of the model which can be shown to be in the class of *weakly* fragmented systems using analytic techniques. Further, the certain fragments have excitations which are highly constrained to move in two spatial dimensions *smaller* than the original dimension of the system. The presence and absence of these fractonic excitations produce different dynamical behavior, which we have also characterized using numerics on small lattices. We emphasize that we have given results showing this geometric fragmentation that are valid on large lattices and indeed in the thermodynamic limit. For fragmentation sectors which are dominated by fractons, we provide analytical solutions for eigenvalues and eigenvectors.

Several general consequences are obvious from our study. In particular, all the statements about the fragmentation in Sec. III A were made for the cubic dimer model, which uses the Gauss sector where we have doped the system with staggered $Q = \pm 1$. These results are also true for the Gauss charge zero sector, $Q = 0$. In that sector, again, maximal flux restricts the action of the Hamiltonian to 2D planes orthogonal to the maximal flux, and the difference is that these 2D lattices do not have charges in this case. The construction of the fragmented subspaces and the weak fragmentation of the $W_x^{3D} = W_y^{3D} = 0$ sector for all choices of L_x and L_y for maximal flux in L_z direction hold true for this charge sector and can be generalized from our study.

It is easy to imagine various interesting directions of research emerging from our study. Are there other regimes possible in the pure gauge theory when other kinds of fragmentation emerge? It is also easy to imagine making the charges dynamical in a controlled fashion by endowing them with a large but finite mass. While winding numbers are not exact symmetries in the presence of charges, one can start with an initial state with a large flux and observe how the total flux evolves in time. This will clearly depend on the phase of the quenching Hamiltonian: a confined phase may try to keep the fluxes around for longer, while in a Coulomb phase fluxes may dissipate by string breaking and recombination. In either case, exotic dynamical and athermal behavior can be expected.

ACKNOWLEDGMENTS

We would like to thank Arnab Sen for comments and discussions, particularly on the use of entropy density as a diagnostic to distinguish between different fragmentation classes. D. B. would like to thank STFC (UK) consolidated Grant No. ST/X000583/1 and continued support from the Alexander von Humboldt Foundation (Germany) in the context of the research fellowship for experienced researchers. Research at Perimeter Institute is supported in part by the Government of Canada through the Department of Innovation, Science and Industry Canada and by the Province of Ontario through the Ministry of Colleges and Universities. This work was supported in part by the Helmholtz Association and the DLR via the Helmholtz Young Investigator Group "DataMat."

DATA AVAILABILITY

The data are not publicly available. The data are available from the authors upon reasonable request.

[1] J. M. Deutsch, Quantum statistical mechanics in a closed system, Phys. Rev. A **43**, 2046 (1991).

[2] M. Srednicki, Chaos and quantum thermalization, Phys. Rev. E **50**, 888 (1994).

[3] M. Rigol, V. Dunjko, and M. Olshanii, Thermalization and its mechanism for generic isolated quantum systems, Nature (London) **452**, 854 (2008).

[4] L. D'Alessio, Y. Kafri, A. Polkovnikov, and M. Rigol, From quantum chaos and eigenstate thermalization to statistical mechanics and thermodynamics, Adv. Phys. **65**, 239 (2016).

[5] G. D. Tomasi, D. Hetterich, P. Sala, and F. Pollmann, Dynamics of strongly interacting systems: From Fock-space fragmentation to many-body localization, Phys. Rev. B **100**, 214313 (2019).

[6] F. Alet and N. Laflorencie, Many-body localization: An introduction and selected topics, C. R. Phys. **19**, 498 (2018).

[7] H. Bernien, S. Schwartz, A. Keesling, H. Levine, A. Omran, H. Pichler, S. Choi, A. S. Zibrov, M. Endres, M. Greiner *et al.*, Probing many-body dynamics on a 51-atom quantum simulator, Nature (London) **551**, 579 (2017).

[8] C. J. Turner, A. A. Michailidis, D. A. Abanin, M. Serbyn, and Z. Papić, Weak ergodicity breaking from quantum many-body scars, Nat. Phys. **14**, 745 (2018).

[9] C. J. Turner, A. A. Michailidis, D. A. Abanin, M. Serbyn, and Z. Papić, Quantum scarred eigenstates in a Rydberg atom chain: Entanglement, breakdown of thermalization, and stability to perturbations, Phys. Rev. B **98**, 155134 (2018).

[10] S. Choi, C. J. Turner, H. Pichler, W. W. Ho, A. A. Michailidis, Z. Papić, M. Serbyn, M. D. Lukin, and D. A. Abanin, Emergent su(2) dynamics and perfect quantum many-body scars, Phys. Rev. Lett. **122**, 220603 (2019).

[11] S. Sachdev, K. Sengupta, and S. M. Girvin, Mott insulators in strong electric fields, Phys. Rev. B **66**, 075128 (2002).

[12] F. M. Surace, P. P. Mazza, G. Giudici, A. Lerose, A. Gambassi, and M. Dalmonte, Lattice gauge theories and string dynamics in Rydberg atom quantum simulators, Phys. Rev. X **10**, 021041 (2020).

[13] D. Banerjee, M. Dalmonte, M. Muller, E. Rico, P. Stebler, U. J. Wiese, and P. Zoller, Atomic quantum simulation of dynamical gauge fields coupled to fermionic matter: From string breaking to evolution after a quench, Phys. Rev. Lett. **109**, 175302 (2012).

[14] Y.-P. Huang, D. Banerjee, and M. Heyl, Dynamical quantum phase transitions in $U(1)$ quantum link models, Phys. Rev. Lett. **122**, 250401 (2019).

[15] A. Chandran, T. Iadecola, V. Khemani, and R. Moessner, Quantum many-body scars: A quasiparticle perspective, Annu. Rev. Condens. Matter Phys. **14**, 443 (2023).

[16] A. Pizzi, B. Evrard, C. B. Dag, and J. Knolle, Quantum scars in many-body systems, Nat. Commun. **16**, 6722 (2025).

[17] N. Shiraishi and T. Mori, Systematic construction of counterexamples to the eigenstate thermalization hypothesis, Phys. Rev. Lett. **119**, 030601 (2017).

[18] M. Schulz, C. A. Hooley, R. Moessner, and F. Pollmann, Stark many-body localization, Phys. Rev. Lett. **122**, 040606 (2019).

[19] F. M. Surace, M. Votto, E. G. Lazo, A. Silva, M. Dalmonte, and G. Giudici, Exact many-body scars and their stability in constrained quantum chains, Phys. Rev. B **103**, 104302 (2021).

[20] J. Wildeboer, A. Seidel, N. S. Srivatsa, A. E. B. Nielsen, and O. Erten, Topological quantum many-body scars in quantum dimer models on the kagome lattice, Phys. Rev. B **104**, L121103 (2021).

[21] B. Mukherjee, S. Nandy, A. Sen, D. Sen, and K. Sengupta, Collapse and revival of quantum many-body scars via Floquet engineering, Phys. Rev. B **101**, 245107 (2020).

[22] B. Mukherjee, A. Sen, D. Sen, and K. Sengupta, Dynamics of the vacuum state in a periodically driven Rydberg chain, Phys. Rev. B **102**, 075123 (2020).

[23] M. Serbyn, D. A. Abanin, and Z. Papić, Quantum many-body scars and weak breaking of ergodicity, Nat. Phys. **17**, 675 (2021).

[24] S. Moudgalya, B. A. Bernevig, and N. Regnault, Quantum many-body scars and Hilbert space fragmentation: A review of exact results, Rep. Prog. Phys. **85**, 086501 (2022).

[25] S. Moudgalya and O. I. Motrunich, Exhaustive characterization of quantum many-body scars using commutant algebras, Phys. Rev. X **14**, 041069 (2024).

[26] A. Udupa, S. Sur, S. Nandy, A. Sen, and D. Sen, Weak universality, quantum many-body scars, and anomalous infinite-temperature autocorrelations in a one-dimensional spin model with duality, Phys. Rev. B **108**, 214430 (2023).

[27] A. Lerose, T. Parolini, R. Fazio, D. A. Abanin, and S. Pappalardi, Theory of robust quantum many-body scars in long-range interacting systems, Phys. Rev. X **15**, 011020 (2025).

[28] M. Pal, M. Sarkar, K. Sengupta, and A. Sen, Scar-induced imbalance in staggered Rydberg ladders, Phys. Rev. B **111**, L161101 (2025).

[29] K. Pakrouski, P. N. Pallegar, F. K. Popov, and I. R. Klebanov, Many-body scars as a group invariant sector of Hilbert space, Phys. Rev. Lett. **125**, 230602 (2020).

[30] K. Pakrouski, P. N. Pallegar, F. K. Popov, and I. R. Klebanov, Group theoretic approach to many-body scar states in fermionic lattice models, Phys. Rev. Res. **3**, 043156 (2021).

[31] S. Moudgalya, N. Regnault, and B. A. Bernevig, η-pairing in Hubbard models: From spectrum generating algebras to quantum many-body scars, Phys. Rev. B **102**, 085140 (2020).

[32] F. Schindler, N. Regnault, and B. A. Bernevig, Exact quantum scars in the chiral nonlinear Luttinger liquid, Phys. Rev. B **105**, 035146 (2022).

[33] P. Kolb and K. Pakrouski, Stability of the many-body scars in fermionic spin-$1/2$ models, PRX Quantum **4**, 040348 (2023).

[34] D. Banerjee and A. Sen, Quantum scars from zero modes in an Abelian lattice gauge theory on ladders, Phys. Rev. Lett. **126**, 220601 (2021).

[35] S. Biswas, D. Banerjee, and A. Sen, Scars from protected zero modes and beyond in $U(1)$ quantum link and quantum dimer models, SciPost Phys. **12**, 148 (2022).

[36] A. S. Aramthottil, U. Bhattacharya, D. González-Cuadra, M. Lewenstein, L. Barbiero, and J. Zakrzewski, Scar states in deconfined F_2 lattice gauge theories, Phys. Rev. B **106**, L041101 (2022).

[37] J. C. Halimeh, L. Barbiero, P. Hauke, F. Grusdt, and A. Bohrdt, Robust quantum many-body scars in lattice gauge theories, Quantum **7**, 1004 (2023).

[38] J.-Y. Desaules, D. Banerjee, A. Hudomal, Z. Papić, A. Sen, and J. C. Halimeh, Weak ergodicity breaking in the Schwinger model, Phys. Rev. B **107**, L201105 (2023).

[39] J.-Y. Desaules, A. Hudomal, D. Banerjee, A. Sen, Z. Papić, and J. C. Halimeh, Prominent quantum many-body scars in a truncated Schwinger model, Phys. Rev. B **107**, 205112 (2023).

[40] T. Hayata and Y. Hidaka, String-net formulation of Hamiltonian lattice Yang-Mills theories and quantum many-body scars in a nonAbelian gauge theory, J. High Energy Phys. 09 (2023) 126.

[41] T. Budde, M. Krstić Marinković, and J. C. P. Barros, Quantum many-body scars for arbitrary integer spin in $2+1$D Abelian gauge theories, Phys. Rev. D **110**, 094506 (2024).

[42] J. Osborne, I. P. McCulloch, and J. C. Halimeh, Quantum many-body scarring in $2+1$D gauge theories with dynamical matter, arXiv:2403.08858.

[43] G. Calajò, G. Cataldi, M. Rigobello, D. Wanisch, G. Magnifico, P. Silvi, S. Montangero, and J. C. Halimeh, Quantum many-body scarring in a non-Abelian lattice gauge theory, Phys. Rev. Res. **7**, 013322 (2025).

[44] I. Sau, D. Banerjee, and A. Sen, Fate of many-body localization in an Abelian lattice gauge theory, arXiv: 2405.20379.

[45] M. Brenes, M. Dalmonte, M. Heyl, and A. Scardicchio, Many-body localization dynamics from gauge invariance, Phys. Rev. Lett. **120**, 030601 (2018).

[46] A. Smith, J. Knolle, D. L. Kovrizhin, and R. Moessner, Disorder-free localization, Phys. Rev. Lett. **118**, 266601 (2017).

[47] P. A. McClarty, M. Haque, A. Sen, and J. Richter, Disorder-free localization and many-body quantum scars from magnetic frustration, Phys. Rev. B **102**, 224303 (2020).

[48] P. Karpov, R. Verdel, Y.-P. Huang, M. Schmitt, and M. Heyl, Disorder-free localization in an interacting 2D lattice gauge theory, Phys. Rev. Lett. **126**, 130401 (2021).

[49] J. Osborne, I. P. McCulloch, and J. C. Halimeh, Disorder-free localization in $2+1$D lattice gauge theories with dynamical matter, arXiv:2301.07720.

[50] J. Jeyaretnam, T. Bhore, J. J. Osborne, J. C. Halimeh, and Z. Papić, Hilbert space fragmentation at the origin of disorder-free localization in the lattice Schwinger model, Commun. Phys. **8**, 172 (2025).

[51] P. Sala, T. Rakovszky, R. Verresen, M. Knap, and F. Pollmann, Ergodicity breaking arising from Hilbert space fragmentation in dipole-conserving Hamiltonians, Phys. Rev. X **10**, 011047 (2020).

[52] V. Khemani, M. Hermele, and R. Nandkishore, Localization from Hilbert space shattering: From theory to physical realizations, Phys. Rev. B **101**, 174204 (2020).

[53] B. Mukherjee, D. Banerjee, K. Sengupta, and A. Sen, Minimal model for Hilbert space fragmentation with local constraints, Phys. Rev. B **104**, 155117 (2021).

[54] K. Lee, A. Pal, and H. J. Changlani, Frustration-induced emergent Hilbert space fragmentation, Phys. Rev. B **103**, 235133 (2021).

[55] A. Chattopadhyay, B. Mukherjee, K. Sengupta, and A. Sen, Strong Hilbert space fragmentation via emergent quantum drums in two dimensions, SciPost Phys. **14**, 146 (2023).

[56] A. Khudorozhkov, A. Tiwari, C. Chamon, and T. Neupert, Hilbert space fragmentation in a 2D quantum spin system with subsystem symmetries, SciPost Phys. **13**, 098 (2022).

[57] S. Ghosh, K. Sengupta, and I. Paul, Hilbert space fragmentation imposed real spectrum of non-Hermitian systems, Phys. Rev. B **109**, 045145 (2024).

[58] A. N. Ciavarella, C. W. Bauer, and J. C. Halimeh, Generic Hilbert space fragmentation in Kogut–Susskind lattice gauge theories, Phys. Rev. D **112**, L091501 (2025).

[59] Y. H. Kwan, P. H. Wilhelm, S. Biswas, and S. A. Parameswaran, Minimal Hubbard models of maximal Hilbert space fragmentation, Phys. Rev. Lett. **134**, 010411 (2025).

[60] P. H. Harkema, M. Iversen, and A. E. B. Nielsen, Hilbert space fragmentation from lattice geometry, Phys. Rev. A **110**, 023301 (2024).

[61] C. Stahl, O. Hart, and R. Nandkishore, Towards absolutely stable ergodicity breaking in two and three dimensions, Phys. Rev. B **111**, L020302 (2025).

[62] D. S. Rokhsar and S. A. Kivelson, Superconductivity and the quantum hard-core dimer gas, Phys. Rev. Lett. **61**, 2376 (1988).

[63] S. A. Kivelson, D. S. Rokhsar, and J. P. Sethna, Topology of the resonating valence-bond state: Solitons and high-T_c superconductivity, Phys. Rev. B **35**, 8865 (1987).

[64] R. Moessner and S. L. Sondhi, Three-dimensional resonating-valence-bond liquids and their excitations, Phys. Rev. B **68**, 184512 (2003).

[65] J. Bonča, S. Maekawa, and T. Tohyama, Numerical approach to the low-doping regime of the $t-j$ model, Phys. Rev. B **76**, 035121 (2007).

[66] M. Hermele, M. P. A. Fisher, and L. Balents, Pyrochlore photons: The U(1) spin liquid in a $S=1/2$ three-dimensional frustrated magnet, Phys. Rev. B **69**, 064404 (2004).

[67] A. Banerjee, S. V. Isakov, K. Damle, and Y. B. Kim, Unusual liquid state of hard-core bosons on the pyrochlore lattice, Phys. Rev. Lett. **100**, 047208 (2008).

[68] O. Sikora, F. Pollmann, N. Shannon, K. Penc, and P. Fulde, Quantum liquid with deconfined fractional excitations in three dimensions, Phys. Rev. Lett. **103**, 247001 (2009).

[69] O. Sikora, N. Shannon, F. Pollmann, K. Penc, and P. Fulde, Extended quantum $u(1)$-liquid phase in a three-dimensional quantum dimer model, Phys. Rev. B **84**, 115129 (2011).

[70] M. J. P. Gingras and P. A. McClarty, Quantum spin ice: A search for gapless quantum spin liquids in pyrochlore magnets, Rep. Prog. Phys. **77**, 056501 (2014).

[71] O. Benton, O. Sikora, and N. Shannon, Seeing the light: Experimental signatures of emergent electromagnetism in a quantum spin ice, Phys. Rev. B **86**, 075154 (2012).

[72] K. A. Ross, L. Savary, B. D. Gaulin, and L. Balents, Quantum excitations in quantum spin ice, Phys. Rev. X **1**, 021002 (2011).

[73] C. Castelnovo, R. Moessner, and S. L. Sondhi, Spin ice, fractionalization, and topological order, Annu. Rev. Condens. Matter Phys. **3**, 35 (2012).

[74] J. Shah, G. Nambiar, A. V. Gorshkov, and V. Galitski, Quantum spin ice in three-dimensional Rydberg atom arrays, Phys. Rev. X **15**, 011025 (2025).

[75] D. Horn, Finite matrix models with continuous local gauge invariance, Phys. Lett. **100B**, 149 (1981).

[76] P. Orland and D. Rohrlich, Lattice gauge magnets: Local isospin from spin, Nucl. Phys. **B338**, 647 (1990).

[77] S. Chandrasekharan, Quantum link models: A discrete approach to gauge theories, Nucl. Phys. **B492**, 455 (1997).

[78] R. Brower, S. Chandrasekharan, and U. J. Wiese, QCD as a quantum link model, Phys. Rev. D **60**, 094502 (1999).

[79] H. Liu and S. Chandrasekharan, Qubit regularization and qubit embedding algebras, Symmetry **14**, 305 (2022).

[80] D. Berenstein, H. Kawai, and R. Brower, U(1) fields from qubits: An approach via D-theory algebra, Phys. Rev. D **110**, 014506 (2024).

[81] K. G. Wilson, Confinement of quarks, Phys. Rev. D **10**, 2445 (1974).

[82] J. Kogut and L. Susskind, Hamiltonian formulation of Wilson's lattice gauge theories, Phys. Rev. D **11**, 395 (1975).

[83] D. Banerjee, F. J. Jiang, P. Widmer, and U. J. Wiese, The $(2+1)$-d U(1) quantum link model masquerading as deconfined criticality, J. Stat. Mech. (2013) P12010.

[84] D. Banerjee, M. Bögli, C. P. Hofmann, F.-J. Jiang, P. Widmer, and U.-J. Wiese, Interfaces, strings, and a soft mode in the square lattice quantum dimer model, Phys. Rev. B **90**, 245143 (2014).

[85] F. Tschirsich, S. Montangero, and M. Dalmonte, Phase diagram and conformal string excitations of square ice using gauge invariant matrix product states, SciPost Phys. **6**, 028 (2019).

[86] G. Magnifico, T. Felser, P. Silvi, and S. Montangero, Lattice quantum electrodynamics in $(3+1)$-dimensions at finite density with tensor networks, Nat. Commun. **12**, 3600 (2021).

[87] D. Banerjee, Recent progress on cluster and meron algorithms for strongly correlated systems, Indian J. Phys. **95**, 1669 (2021).

[88] S. Chandrasekharan, R. X. Siew, and T. Bhattacharya, Monomer-dimer tensor-network basis for qubit-regularized lattice gauge theories, Phys. Rev. D **111**, 114502 (2025).

[89] D. González-Cuadra, E. Zohar, and J. I. Cirac, Quantum simulation of the Abelian-Higgs lattice gauge theory with ultracold atoms, New J. Phys. **19**, 063038 (2017).

[90] J. Bender, E. Zohar, A. Farace, and J. I. Cirac, Digital quantum simulation of lattice gauge theories in three spatial dimensions, New J. Phys. **20**, 093001 (2018).

[91] R. Ott, T. V. Zache, F. Jendrzejewski, and J. Berges, Scalable cold-atom quantum simulator for two-dimensional QED, Phys. Rev. Lett. **127**, 130504 (2021).

[92] M. C. Bañuls, R. Blatt, J. Catani, A. Celi, J. I. Cirac, M. Dalmonte, L. Fallani, K. Jansen, M. Lewenstein, S. Montangero *et al.*, Simulating lattice gauge theories within quantum technologies, Eur. Phys. J. D **74**, 165 (2020).

[93] J. C. Halimeh, M. Aidelsburger, F. Grusdt, P. Hauke, and B. Yang, Cold-atom quantum simulators of gauge theories, Nat. Phys. **21**, 25 (2025).

[94] C. W. Bauer, Z. Davoudi, N. Klco, and M. J. Savage, Quantum simulation of fundamental particles and forces, Nat. Rev. Phys. **5**, 420 (2023).

[95] D. Banerjee, E. Huffman, and L. Rammelmüller, Exploring bosonic and fermionic link models on $(3+1)$D tubes, Phys. Rev. Res. **4**, 033174 (2022).

[96] T. V. Zache, M. V. Damme, J. C. Halimeh, P. Hauke, and D. Banerjee, Towards the continuum limit of a $(1+1)$d quantum link Schwinger model, Phys. Rev. D **106**, L091502 (2022).

[97] See Supplemental Material at http://link.aps.org/supplemental/10.1103/4kzq-t1zs for a generalized fragmentation proof, a proof of weak fragmentation in nonzero-winding sectors, and examples illustrating constructions of fractonic winding sectors.

[98] S.-L. Lee, Y.-L. Luo, B. E. Sagan, and Y.-N. Yeh, Eigenvector and eigenvalues of some special graphs. IV. Multilevel circulants, Int. J. Quantum Chem. **41**, 105 (1992).